



Structure and Electrochemistry of $\text{LiNi}_{1/3}\text{Co}_{1/3-y}\text{M}_y\text{Mn}_{1/3}\text{O}_2$ (M = Ti, Al, Fe) Positive Electrode Materials

James Wilcox,^{a,b,*} Sébastien Patoux,^c and Marca Doeff^{a,*,z}

^aMaterials Sciences Division and ^bDepartment of Materials Science and Engineering,
University of California, Berkeley, California 94720, USA

^cLaboratoire d'Innovation pour les Technologies des Energies Nouvelles, Commissariat à l'Energie Atomique (CEA), 38054 Grenoble Cedex 9, France

A series of materials based on the $\text{LiNi}_{1/3}\text{Co}_{1/3-y}\text{M}_y\text{Mn}_{1/3}\text{O}_2$ (M = Ti, Al, Fe) system has been synthesized and examined structurally and electrochemically. It is found that the changes in electrochemical performance depend highly on the nature of the substituting atom and its effect on the crystal structure. Substitution with small amounts of Ti^{4+} ($y = 1/12$) leads to the formation of a high-capacity and high-rate positive electrode material. Iron substituted materials suffer from an increased antisite defect concentration and exhibit lower capacities and poor rate capabilities. Single-phase materials are found for $\text{LiNi}_{1/3}\text{Co}_{1/3-y}\text{Al}_y\text{Mn}_{1/3}\text{O}_2$ when $y \leq 1/4$ and all exhibit decreased capacities when cycled to 4.3 V. However, an increase in rate performance and cycle stability upon aluminum substitution is correlated with an improved lamellar structure.
© 2009 The Electrochemical Society. [DOI: 10.1149/1.3056109] All rights reserved.

Manuscript submitted September 15, 2008; revised manuscript received November 23, 2008. Published January 15, 2009.

A significant amount of research has been directed at finding positive electrode materials with high capacity as well as low cost and toxicity to replace LiCoO_2 . Of particular interest is the series of materials, $\text{LiNi}_{1-y-z}\text{Co}_y\text{Mn}_z\text{O}_2$, which potentially combines the rate performance of LiCoO_2 , the high capacity of LiNiO_2 , and the structural stabilization imparted by the presence of Mn^{4+} .^{1,2} Specifically, $\text{LiNi}_{1/3}\text{Co}_{1/3}\text{Mn}_{1/3}\text{O}_2$ has garnered much attention and has been shown to deliver 150 mAh/g between 2.5 and 4.2 V vs lithium and close to 200 mAh/g when the charge potential limit is increased to 4.6 V.³⁻⁷ In addition, $\text{LiNi}_{1/3}\text{Co}_{1/3}\text{Mn}_{1/3}\text{O}_2$ possesses excellent power characteristics, exceeding the high-power pulse requirement for hybrid vehicle applications,⁸ and increased thermal abuse tolerance compared to $\text{LiNi}_{0.8}\text{Co}_{0.15}\text{Al}_{0.05}\text{O}_2$.⁹

The inherent improvements in rate capability of $\text{LiNi}_{1/3}\text{Co}_{1/3}\text{Mn}_{1/3}\text{O}_2$ over other oxide materials, including $\text{LiNi}_{0.5}\text{Mn}_{0.5}\text{O}_2$ produced using traditional methods,¹⁰⁻¹² is due largely to the structural properties associated with the presence of cobalt. AMO₂-type materials with the highly layered α - NaFeO_2 structure (space group $R\bar{3}m$), where A is typically Li^+ and M is a metal 3+ cation, are stabilized for metal ions with an ionic radius substantially smaller than that of lithium (0.76 Å).^{13,14} Because of the small ionic radius of low spin Co^{3+} (0.545 Å), the incorporation of cobalt into the crystal lattice minimizes antisite cation defect concentrations leading to facile lithium-ion transport.¹⁴⁻¹⁸

To create electrode materials with further reduced cobalt contents and lower antisite defect concentrations, while avoiding effective but complicated ion exchange pathways,¹⁹ substitutive elements should promote the formation of a lamellar structure through either steric or chemical interactions. Iron, which has an ionic radius of 0.645 Å in the low spin state, is an attractive replacement for cobalt due to its low cost and toxicity. However, the native lithiated oxide, LiFeO_2 , is not layered like α - NaFeO_2 but has an ordered tetragonal structure (γ - LiFeO_2 , space group $I4_1/amd$).^{20,21} Accordingly, substitution into the layered oxide materials has been limited to relatively low levels. $\text{LiNi}_{1/3}\text{Co}_{1/6}\text{Fe}_{1/6}\text{Mn}_{1/3}\text{O}_2$, synthesized using a sol-gel synthesis method delivers ~150 mAh/g between 3.0 and 4.5 V vs Li/Li^+ , although a ~20% capacity fade within the first 30 cycles was observed.²²

A previous report on the selective replacement of cobalt with aluminum in the series $\text{LiNi}_{1/3}\text{Al}_{1/3-x}\text{Co}_x\text{Mn}_{1/3}\text{O}_2$ indicates that single-phase materials are formed for $1/6 \leq x \leq 1/3$.²³ Interestingly, even given the small ionic radius of the Al^{3+} ion (0.545 Å),

an increase in the cation mixing was observed. This was connected with an increased cell polarization and limited capacity below 4.5 V (~120 mAh/g at $x = 0$).

Several different titanium-substituted layered oxides have been reported in the literature including $\text{LiCo}_{1-z}\text{Ti}_z\text{O}_2$ ($z = 0.25, 0.5$),²⁴ $\text{LiNi}_{1-x}\text{Ti}_x\text{O}_2$ ($0 \leq x \leq 0.1, 0.5$),^{25,26} $\text{LiNi}_{0.8-y}\text{Ti}_y\text{Co}_{0.2}\text{O}_2$ ($0 \leq y \leq 0.1$),²⁷ and $\text{LiNi}_{0.8}\text{Ti}_{0.1}\text{Co}_{0.1}\text{O}_2$.²⁸ In most cases, it was found that the incorporation of titanium leads to improved reversibility and thermal stability. The structural effects of titanium substitution remain unclear, however, with both increasing and decreasing antisite defect concentrations being reported. This is not surprising because, depending on the chemistry involved, substitution with Ti^{4+} may lead to the formation of a Ni^{2+} component for charge compensation. Divalent nickel has a strong propensity to migrate to the lithium 3b site and may account for at least some of the disparities reported experimentally.

The goal of this work is to understand the systematic changes caused by substitution of Fe^{3+} , Al^{3+} , and Ti^{4+} for Co^{3+} in $\text{LiNi}_{1/3}\text{Co}_{1/3-y}\text{M}_y\text{Mn}_{1/3}\text{O}_2$, for compositions leading to single-phase materials. The effect of these substitutions on the crystallographic parameters, cycle life, and rate performance are discussed.

Experimental

The glycine nitrate combustion (GNC) process was used for the synthesis of all oxide active materials used in this study.^{29,30} Aqueous solutions of LiNO_3 (Mallinckrodt), $\text{Mn}(\text{NO}_3)_2$ (45–50 wt % in dilute nitric acid, Sigma Aldrich), $\text{Co}(\text{NO}_3)_2 \cdot 6\text{H}_2\text{O}$ (98%, Sigma Aldrich), $\text{Ni}(\text{NO}_3)_2 \cdot 6\text{H}_2\text{O}$ (Sigma Aldrich), $\text{Al}(\text{NO}_3)_3 \cdot 9\text{H}_2\text{O}$ (98 + %, Sigma Aldrich), $\text{Fe}(\text{NO}_3)_3 \cdot 9\text{H}_2\text{O}$ (98% EMD), and $\text{TiO}(\text{NO}_3)_2$ and glycine (98.5 + %, Sigma Aldrich) corresponding to the desired stoichiometry were combined in a stainless steel combustion chamber. The solution was then concentrated on a hot plate until auto ignition occurred. $\text{TiO}(\text{NO}_3)_2$ was prepared via the hydrolysis of TiCl_4 (99.9%, Sigma Aldrich) with ammonia and subsequent reaction with nitric acid (69%, BDH).³¹ For comparison purposes, a constant glycine to nitrate ratio of 0.5 was used for all materials corresponding to a combustion temperature of about 1350°C.²⁹ After combustion, powders were planetary ballmilled for 1 h in acetone and dried under flowing nitrogen before being fired at 800°C (4°C/min heating rate) for 4 h in air.

Powder X-ray diffraction (XRD) was performed on a Phillips X'Pert diffractometer with an X'celerator detector using $\text{Cu K}\alpha$ radiation. A back-loading powder holder was used to minimize the impact of any preferred orientation. Unit cell parameters were obtained from Rietveld refinement using the WINPLOTR/FullProf

* Electrochemical Society Student Member.

** Electrochemical Society Active Member.

^z E-mail: mmdoeff@lbl.gov

suite.³² Particle morphology studies were conducted using a field-emission scanning electron microscope [(SEM), JEOL JSM-6340F].

Laminate composite electrodes comprised of 84 wt % active material, 8 wt % poly(vinylidene fluoride) (Kureha Chemical Ind. Co. Limited), 4 wt % compressed acetylene black, and 4 wt % SFG-6 synthetic flake graphite (Timcal Ltd., Graphites and Technologies) were prepared by applying slurries in 1-methyl-2-pyrrolidinone onto carbon-coated current collectors (Intelicoat Technologies) by automated doctor blade. After drying in air and in vacuum for at least 24 h, 1.8 cm² electrodes having an average loading of 7–10 mg/cm² of active material were punched out. Coin cells (2032) were assembled in a helium-filled glove box with lithium metal anodes and 1 M LiPF₆ in 1:2 ethylene carbonate/dimethyl carbonate electrolyte solution (Ferro). Galvanostatic cycling was carried out on an Arbin BT/HSP-2043 cycler between limits of 2.0 and 4.3–4.7 V. All cells were charged at a current density of 0.1 mA/cm² independent of the discharge rate.

Results and Discussion

The impact of substitution for cobalt in layered oxide systems upon electrochemical performance will vary depending on the nature of the substituting atom. Because cobalt does not become electroactive until potentials exceed 4.3 V, much of the capacity related to the Co^{3+/4+} redox couple is not utilized under normal cycling conditions.^{33,34} Therefore, the effect on practical capacities should be minimal as long as no other properties, such as ionic or electronic conductivity or voltage characteristics, are grossly affected by the substitution. This is significant because it may allow for the substitution of cobalt with electrochemically inactive species, such as Al³⁺, that lower the theoretical capacity (e.g., 208 mAh/g for LiNi_{1/3}Al_{1/3}Mn_{1/3}O₂) compared to the parent material, LiNi_{1/3}Co_{1/3}Mn_{1/3}O₂ (278 mAh/g). Aliovalent substitution with Ti⁴⁺ requires the reduction of the redox state of another transition metal species to maintain charge neutrality. The most probable charge balance reaction is partial reduction of Mn⁴⁺ to Mn³⁺. Mn³⁺ is electroactive in the window of 3–3.5 V,³⁵ and can compensate for the inactivity of Ti⁴⁺. Therefore, a slight increase in theoretical capacity is expected (289 mAh/g) for the hypothetical LiNi_{1/3}Ti_{1/3}Mn_{1/3}O₂ due to the lower atomic weight of Ti compared to Co. (It may, however, be difficult to detect Mn electroactivity at the low substitution levels utilized in this study.)²⁵ Iron-substituted materials have slightly higher theoretical capacities (e.g., 281 mAh/g for the hypothetical LiNi_{1/3}Fe_{1/3}Mn_{1/3}O₂) than the LiNi_{1/3}Co_{1/3}Mn_{1/3}O₂ because of the slightly lower atomic weight of iron and its presumed electroactivity.

In this study, single-phase materials were obtained for all substitutions when *y* was limited to a value of 1/12 in LiNi_{1/3}Co_{1/3-y}M_yMn_{1/3}O₂ (M = Ti, Al, Fe). Substitution of titanium and iron at levels greater than 1/12 leads to the formation of spinel-like impurity phases and will not be discussed further. A higher degree of solubility was observed in the aluminum-substituted system where an impurity phase was observed only for *y* = 1/3.

The primary particle size estimated from Rietveld refinement is approximately 40–50 nm for all samples and agrees well with the particle size (50 nm) observed in transmission electron microscope images of similarly produced oxide powders.³⁰ Figure 1 shows an SEM image of the parent material, LiNi_{1/3}Co_{1/3}Mn_{1/3}O₂, produced using the GNC method and is characteristic of all of the materials used in this study. The agglomeration into secondary particles with a diameter of ~500 nm can be clearly seen and is also typical.

LiNi_{1/3}Co_{1/4}M_{1/12}Mn_{1/3}O₂ (M = Co, Ti, Al, Fe).—The powder XRD patterns presented in Fig. 2 indicate that the substitution of 1/12 of the cobalt content with aluminum, iron, or titanium results

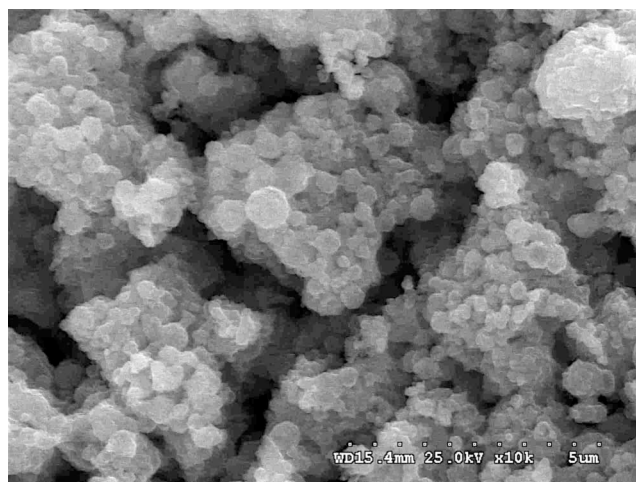


Figure 1. SEM image of LiNi_{1/3}Co_{1/3}Mn_{1/3}O₂ powder produced via the GNC method. Secondary particles with diameters in the range of 500 nm are comprised of ~40 to 50 nm primary particles.

in highly crystalline single-phase powders. All peaks could be indexed in the R $\bar{3}$ m space group with no evidence of a second phase (the 200 peak of the aluminum sample holder is, however, evident in the patterns). The results of the Rietveld refinements are presented in Table I. For the α -NaFeO₂ structure, the *a* lattice parameter is a measure of the distance between metal centers in the transition metal plane and is relatively unaffected by substitution; only a small shift (0.4% maximum) is observed. The experimentally observed trend is readily explained by the minor differences in ionic radii of cobalt (0.545 Å), aluminum (0.535 Å), titanium (0.605 Å), and iron (0.645 Å).¹³ Minor shifts in the *c*-axis are observed upon substitution; the *c* lattice parameter expands to a maximum of 14.298 Å (0.3%) on substitution with the largest ion (Ti).

The overlap of the 200 peak from the aluminum sample holder with the 104 peak of the X-ray patterns in Fig. 2 precluded the implicit refinement of the antisite defect concentration, but the *c*/*3a* ratio has been shown to be a close corollary for many materials.³⁶ The ideal structure with a cubic close-packed framework has a value of 1.633. For materials with the α -NaFeO₂ structure, this ratio increases significantly, approaching 1.793 for an ideal layered material with no ion mixing, such as LiTiS₂.³⁷ LiNi_{1/3}Co_{1/3}Mn_{1/3}O₂ has a *c*/*3a* ratio of 1.660, implying a significant degree of cation mixing. Substitution with aluminum (1.663) and titanium (1.661) leads to an increase in this value and, presumably, reduced antisite defect con-

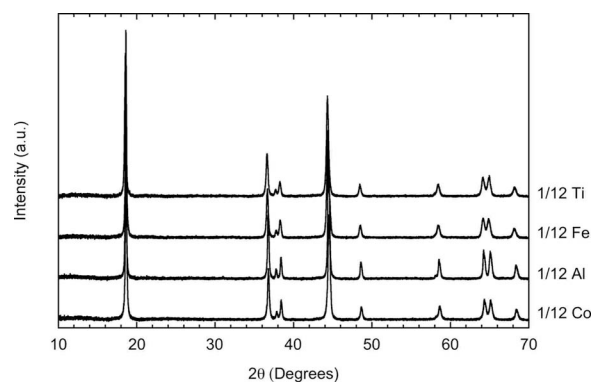


Figure 2. Powder XRD patterns of LiNi_{1/3}Co_{1/4}M_{1/12}Mn_{1/3}O₂ (M = Ti, Fe, Al, and Co). All materials were single phase and could be indexed to the R $\bar{3}$ m space group.

Table I. Structural parameters of $\text{LiNi}_{1/3}\text{Co}_{1/3-y}\text{M}_y\text{Mn}_{1/3}\text{O}_2$ ($\text{M} = \text{Co, Ti, Al, Fe}$) compounds

Transition metal	Substitution level, y	Unit cell parameters		Unit cell volume (\AA^3)	$c/3^a$	z_{Ox}	S (MO_2) (\AA) ^a	I (LiO_2) (\AA) ^a
		a (\AA)	c (\AA)					
Co	1/12	2.862(2)	14.254(1)	101.145(2)	1.660	0.2574(2)	2.16	2.59
Ti	1/12	2.870(2)	14.298(2)	101.996(2)	1.661	0.2582(2)	2.15	2.62
Fe	1/12	2.873(3)	14.275(2)	102.072(2)	1.656	0.2590(2)	2.14	2.62
Al	1/12	2.862(2)	14.281(1)	101.332(2)	1.663	0.2596(2)	2.10	2.66
Al	1/6	2.863(2)	14.285(2)	101.423(2)	1.663	0.2593(2)	2.11	2.65
Al	1/4	2.863(2)	14.292(2)	101.437(2)	1.664	0.2590(2)	2.12	2.64
Al	1/3 ^b	2.863(2)	14.298(2)	101.490(2)	1.665	0.2594(2)	2.11	2.66

^a Transition metal slab spacing (S) and lithium slab spacing (I) as defined in Ref. 47.

^b γ - LiAlO_2 was observed as an impurity in this composition.

tent. In contrast, the $c/3a$ ratio of $\text{LiNi}_{1/3}\text{Co}_{1/4}\text{Fe}_{1/12}\text{Mn}_{1/3}\text{O}_2$ (1.656) is lower than that of the parent compound. This reflects the tendency of materials with high iron content to crystallize in the γ - LiFeO_2 structure, with an ordered arrangement of lithium and iron on the $3a$ and $3b$ crystallographic sites rather than in a lamellar structure. Although large shifts in the $c/3a$ ratio can generally be ascribed to changes in the antisite defect concentration, the dimension of the transition metal layer may also change on substitution with an ion that is different in size than the original. However, the ionic radii of low spin Fe^{3+} , Al^{3+} , and Ti^{4+} are not substantially different from that of Co^{3+} ; thus, the $c/3a$ ratio is expected to primarily reflect changes in the antisite defect concentrations in these materials.

$\text{Li}/\text{LiNi}_{1/3}\text{Co}_{1/4}\text{M}_{1/12}\text{Mn}_{1/3}\text{O}_2$ ($\text{M} = \text{Co, Ti, Al, Fe}$) cells cycled at low current densities ($0.1 \text{ mA}/\text{cm}^2$) between 2.0 and 4.3 V (Fig. 3) show that substitution of even small amounts of cobalt in $\text{LiNi}_{1/3}\text{Co}_{1/3}\text{Mn}_{1/3}\text{O}_2$ has a dramatic effect on the electrochemical performance. Cells containing the parent material or $\text{LiNi}_{1/3}\text{Co}_{1/4}\text{Ti}_{1/12}\text{Mn}_{1/3}\text{O}_2$ deliver $\sim 170 \text{ mAh}/\text{g}$ on the first discharge and cycle with negligible capacity fade. $\text{Li}/\text{LiNi}_{1/3}\text{Co}_{1/4}\text{Al}_{1/12}\text{Mn}_{1/3}\text{O}_2$ cells cycle equally well, but the discharge capacity is decreased by $\sim 11\%$. $\text{Li}/\text{LiNi}_{1/3}\text{Co}_{1/4}\text{Fe}_{1/12}\text{Mn}_{1/3}\text{O}_2$ cells only deliver $142 \text{ mAh}/\text{g}$ initially, and the capacity fades rapidly at a rate of $0.6\%/ \text{cycle}$. This is

similar to previous findings on the effect of Fe substitution in layered transition metal oxides.²¹ X-ray photoelectron spectroscopy experiments and ab initio calculations have shown that iron is electroactive in the same potential window as the $\text{Ni}^{2+/4+}$ redox couple.²² Therefore, the reduced practical capacity is assumed to be a result of kinetic rather than thermodynamic limitations.

Differential capacity plots of the first cycles of the $\text{Li}/\text{LiNi}_{1/3}\text{Co}_{1/4}\text{M}_{1/12}\text{Mn}_{1/3}\text{O}_2$ ($\text{M} = \text{Co, Ti, Al, Fe}$) cells are presented in Fig. 4. All of the dQ/dV plots for the substituted materials show increases in the peak charge and discharge potentials and broader peaks compared to those of the parent compound, indicating that the voltage profiles are modified. This not only serves as a strong indicator that the substitutive elements were incorporated into the host lattice but also shows the effects on the electrochemical potential of lithium-ion insertion and removal. The shift is greatest for the Al-substituted material ($\sim 50 \text{ mV}$) and has been predicted by ab initio calculations.^{23,38-40} In general, the increase in discharge peak potential is less pronounced than for charge, with all of the substituted materials delivering peak capacity near 3.77 V compared to 3.75 V for the unsubstituted analog. The increase in charge potential explains the lower-than-expected practical capacities obtained for several of the substituted materials using a 4.3 V cutoff. Increasing the charge cutoff potential to 4.7 V allows significantly

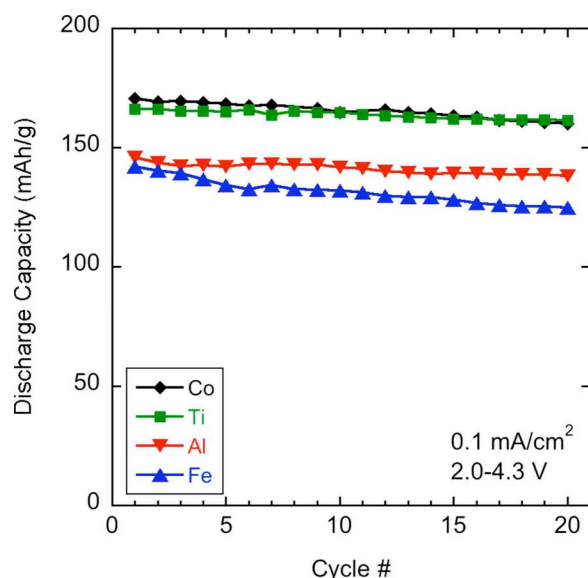


Figure 3. (Color online) Discharge capacities of $\text{Li}/\text{LiNi}_{1/3}\text{Co}_{1/4}\text{M}_{1/12}\text{Mn}_{1/3}\text{O}_2$ ($\text{M} = \text{Ti, Fe, Al, and Co}$) cells. Cycling was limited to 2.0–4.3 V vs Li/Li^+ at a constant charge and discharge current density of $0.1 \text{ mA}/\text{cm}^2$.

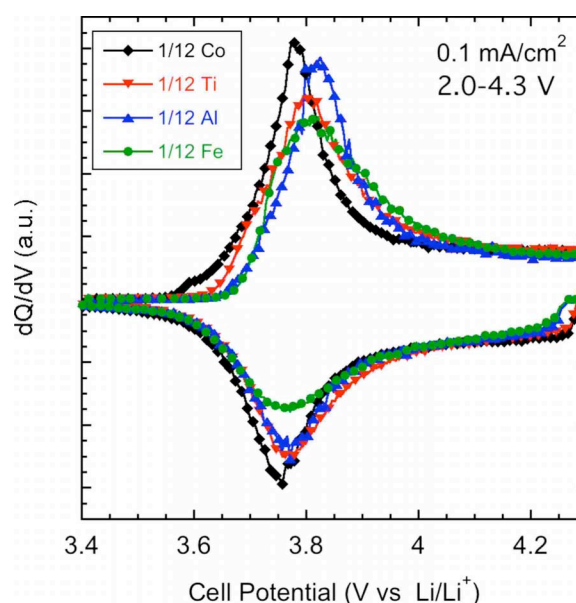


Figure 4. (Color online) Differential capacity plots of the first cycles of $\text{Li}/\text{LiNi}_{1/3}\text{Co}_{1/4}\text{M}_{1/12}\text{Mn}_{1/3}\text{O}_2$ ($\text{M} = \text{Co, Ti, Al, and Fe}$) cells. Current density was $0.1 \text{ mA}/\text{cm}^2$ in the potential range of 2.0–4.3 V vs Li/Li^+ .

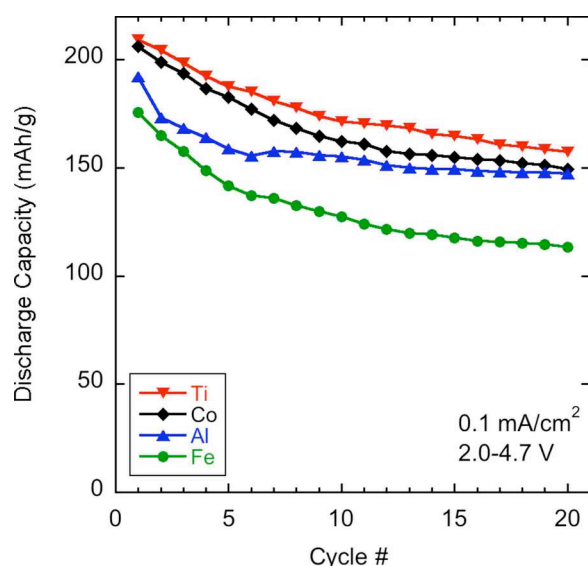


Figure 5. (Color online) Discharge capacities of Li/LiNi_{1/3}Co_{1/4}M_{1/12}Mn_{1/3}O₂ (M = Ti, Fe, Al, and Co) cells. Cycling was limited to 2.0–4.7 V vs Li/Li⁺ at a constant charge and discharge current density of 0.1 mA/cm².

higher utilization of the electrode active materials (Fig. 5) but also results in faster capacity fading, due either to instability of the oxidized active materials or irreversible oxidation of the electrolyte solutions.

The capacities of Li/LiNi_{1/3}Co_{1/4}M_{1/12}Mn_{1/3}O₂ (M = Co, Ti, Al, Fe) cells as a function of current density are shown in Fig. 6. Interestingly, substitution with Al or Ti leads to improved rate capability compared to LiNi_{1/3}Co_{1/3}Mn_{1/3}O₂, particularly at higher current densities. The performance of LiNi_{1/3}Co_{1/4}Ti_{1/12}Mn_{1/3}O₂ is particularly notable, delivering ~95 mAh/g at 6 mA/cm² (~3 C rate). The main structural difference between LiNi_{1/3}Co_{1/3}Mn_{1/3}O₂ and LiNi_{1/3}Co_{1/4}Ti_{1/12}Mn_{1/3}O₂ is the increase in the *c* parameter and

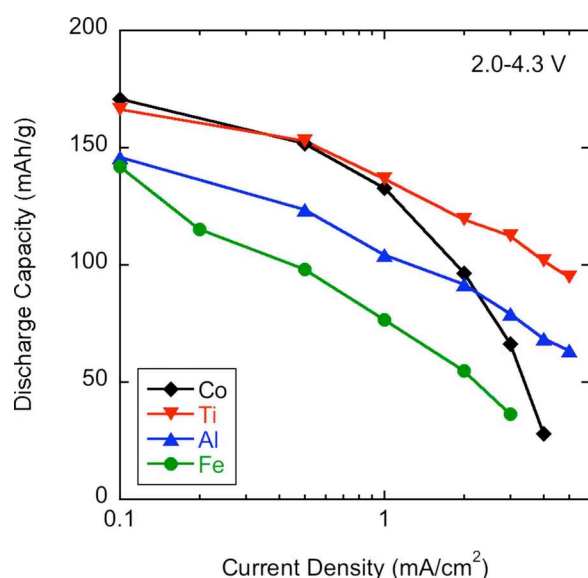


Figure 6. (Color online) Rate capabilities of Li/LiNi_{1/3}Co_{1/4}M_{1/12}Mn_{1/3}O₂ (M = Ti, Fe, Al, and Co) cells. Cycling was limited to 2.0–4.3 V, and a constant charge current density of 0.1 mA/cm² was used.

lithium interslab space caused by partial replacement of Co³⁺ with the Ti⁴⁺ ion. The increased lithium slab dimension leads to enhanced Li-ion diffusion through the adjacent tetrahedral vacancy.¹⁵ In contrast, cells with LiNi_{1/3}Co_{1/4}Fe_{1/12}Mn_{1/3}O₂ have a very poor rate performance with a pronounced reduction in delivered capacity upon even minor increases in the discharge current density.

Figure 7 shows first cycles of lithium cells containing LiNi_{1/3}Co_{1/4}M_{1/12}Mn_{1/3}O₂ (M = Co, Ti, Al, Fe) at 0.1 mA/cm². The irreversible capacity, defined as the difference in first-charge and discharge capacity with respect to the discharge capacity, varies with the nature of the substituent and is lowest for M = Co and highest for M = Fe. High irreversible capacities are undesirable because they can considerably reduce practical energy densities. In nonstoichiometric lithium nickel oxides (Li_{1-z}Ni_{1+z}O₂) large irreversible capacities have been associated with the oxidation of Ni²⁺ ions residing within lithium layers. The oxidation of the extra nickel ions leads to the local collapse of the lithium layer inhibiting the reintercalation of adjacent lithium vacancies except at very low rates.^{41,42} Choi and Manthiram suggest that a parasitic reaction between the active material and electrolyte may be responsible for the irreversibility in cells containing LiNi_{1/3}Co_{1/3}Mn_{1/3}O₂.⁴³ In the same system, Tsai et al. discovered a correlation between irreversible capacity and the inability to reduce all of the Ni⁴⁺ to Ni²⁺ using X-ray absorption near-edge spectroscopy.³⁴ Alternatively, a sudden decrease in lithium-ion mobility at the end of discharge has been observed in LiNi_{1-y}Fe_yO₂ materials.⁴⁴ An associated drop in potential inhibits the complete reinsertion of lithium into the structure, although an overlithiated surface phase may be formed at potentials near 2 V.

The irreversible capacities observed for mixed metal systems are dependent on the voltage limits used and synthesis method and can vary substantially for identical compositions. For example, a 12.9% irreversible capacity is observed in cells with LiNi_{1/3}Co_{1/3}Mn_{1/3}O₂ materials produced via oxalate coprecipitation¹ but only 7% for the material in this study, typical of those made by glycine nitrate combustion.⁴⁵ Titanium substitution does not change this significantly, but aluminum-containing materials suffer from a 13% loss in capacity during the first cycle. The irreversible capacity of the iron-substituted material increases to 23% possibly reflecting the inhibited kinetics associated with the decreased *c*/3*a* ratio of this material and the oxidation of Ni²⁺ in the lithium layers.

Cycling cells to 4.7 V results in a substantial increase in irreversible capacity for all of the positive electrode materials. In cells containing LiNi_{1/3}Co_{1/3}Mn_{1/3}O₂, it doubles to 14%, while there is a nearly threefold increase to 23% for those with LiNi_{1/3}Co_{1/4}Ti_{1/12}Mn_{1/3}O₂ and 31% for LiNi_{1/3}Co_{1/4}Fe_{1/12}Mn_{1/3}O₂. Interestingly, for Li/LiNi_{1/3}Co_{1/4}Al_{1/12}Mn_{1/3}O₂ cells, there is a relatively small increase in irreversible capacity from 13% using a 4.3 V cutoff to just 17% using 4.7 V. In all cases, no evidence of second-phase formation between 2 and 4.3 or 4.7 V was observed.

LiNi_{1/3}Co_{1/3-y}Al_yMn_{1/3}O₂, (1/3 ≥ y ≥ 0).—XRD powder diffraction patterns (Fig. 8) show that highly crystalline, single-phase materials are formed for aluminum contents between 0 ≤ y ≤ 1/4. For y = 1/3, a second phase of γ-LiAlO₂ is detected, consistent with both previous experimental work²³ and as predicted by Buta et al. using ab initio methods⁴⁶ for materials synthesized above 600°C. Refinement of the X-ray patterns indicate that aluminum substitution has a negligible effect on the *a* unit cell parameter but that there is a systematic expansion of the *c* unit cell parameter with increasing aluminum contents (Table I). Correspondingly, the *c*/3*a* ratio increases to 1.665 at y = 1/3 (1.664 for the single-phase material at y = 1/4), indicating an improved lamellar structure on the incorporation of aluminum. This is further substantiated by the increased splitting between the 018 and 110 peaks in the XRD patterns and the shifts in the 003 peaks (Fig. 8 insets). The lithium slab dimension

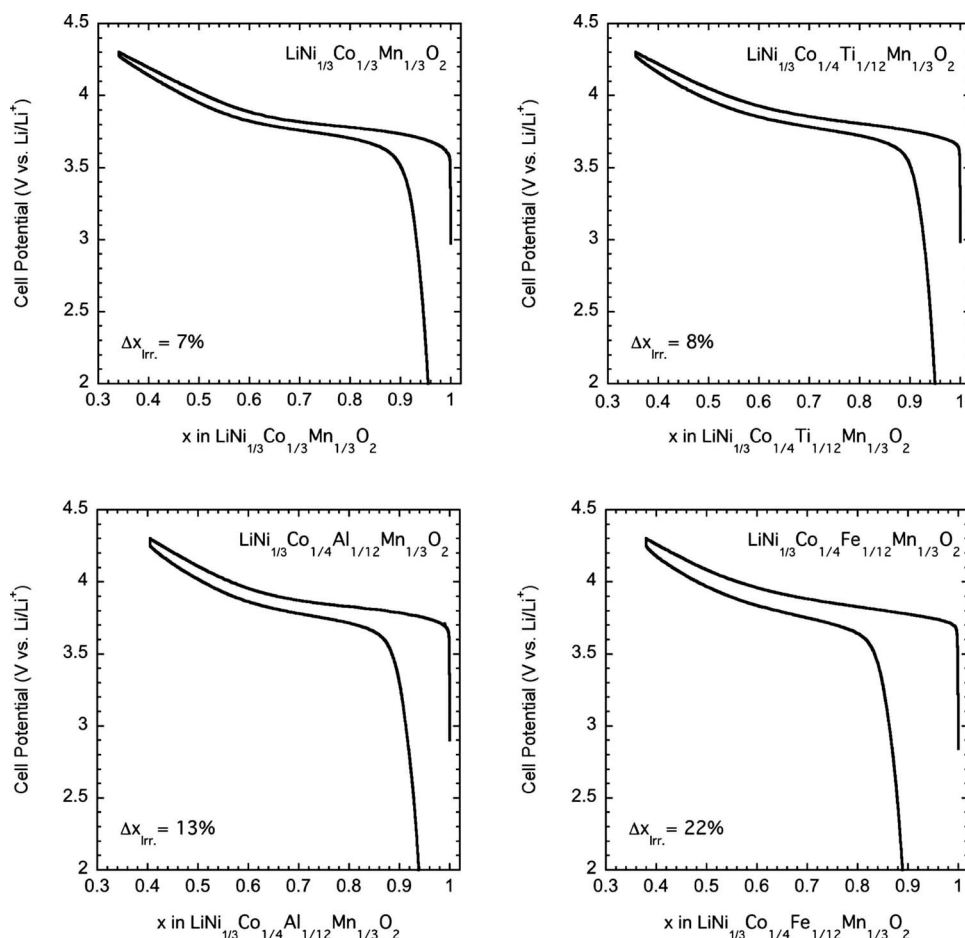


Figure 7. First cycles of Li/LiNi_{1/3}Co_{1/4}M_{1/12}Mn_{1/3}O₂ (M = Ti, Fe, Al, and Co) cells at 0.1 mA/cm² between 2.0 and 4.3 V vs. Li/Li⁺. Irreversible capacities are defined in the text.

increases from 2.59 Å at $y = 0$ to 2.66 Å at $y = 1/3$, implying that the incorporation of aluminum leads to a decrease in the antisite defect concentration.⁴⁷ In contrast, Hu et al.²³ observed an increase in antisite cation defects at elevated aluminum contents. However, the materials in this study were heated to 800°C for a relatively short time (4 h) rather than 900°C. At the higher temperature, there is reduced solubility of aluminum⁴⁶ and more substantial mixing between lithium in the 3b site and transition metals in the 3a position.

The discharge capacities of Li/LiNi_{1/3}Co_{1/3-y}Al_yMn_{1/3}O₂ ($0 \leq y \leq 1/3$) cells cycled between 2.0 and 4.3 V at a low current density (0.1 mA/cm²) are presented in Fig. 9. There is a systematic decrease in the specific capacity as the Al content is increased, as found previously.²³ The source of this phenomenon becomes apparent when looking at the differential capacity plots (Fig. 10). On Al substitution, there is a rise in the oxidation potential, as predicted by first-principles calculations, due to the increased oxygen participation in the redox reaction.⁴⁰ At $y = 1/3$, the peak oxidation potential is located at 3.97 V and is ~200 mV greater than for the parent compound (3.75 V). Thus, the potential required to remove a significant fraction of the lithium from the Al-substituted materials is above the electrolyte oxidative stability threshold of ~4.3 V vs. Li/Li⁺, resulting in reduced practical capacity.

Cycling to 4.7 V leads to higher capacities for all the cells containing LiNi_{1/3}Co_{1/3-y}Al_yMn_{1/3}O₂, ($0 \leq y \leq 1/3$) electrodes (Fig. 11), although the amount of improvement is dependent on the exact composition. For example, there is an increase of only 4% for cells containing LiNi_{1/3}Co_{1/6}Al_{1/6}Mn_{1/3}O₂ active materials when cycling to 4.7 V (145 mAh/g) rather than 4.3 V (139 mAh/g). The higher oxidation potential has a more pronounced effect at all other substitution levels with $y = 0$ (206 mAh/g) delivering 21% more capac-

ity, $y = 1/12$ (192 mAh/g) 32%, $y = 1/4$ (136 mAh/g) 12%, and $y = 1/3$ (123 mAh/g) 24%. Utilization is increased to 74% of the theoretical capacity for materials with $y < 1/6$ cycled to 4.7 V. However, for materials with $y \geq 1/6$, this decreases to 60%, reflecting the shift in the voltage profile caused by the increased Al content. Although capacity and utilization are lower, the cycling behavior improves. At substitution levels of $y \geq 1/6$, virtually no capacity fade is observed after the first cycle. The increased cycling stability may be due, in part, to the inability to completely remove all of the lithium from the structure even at high potentials. Although this lowers the energy density of these materials, it is compensated in part by the increased average cell potential and has been shown to improve the thermal stability of the delithiated oxide.^{36,48,49}

As the rate data presented in Fig. 12 show, the reduced antisite defect concentration and increase in the Li slab dimensions (Table I) associated with Al substitution leads to positive electrode materials with better rate capabilities than the parent compound. All the LiNi_{1/3}Co_{1/3-y}Al_yMn_{1/3}O₂ compounds retain a significantly greater portion of the discharge capacity obtained at low rates when the current is increased, independent of the value of y . However, the decreased capacity obtained at <4.3 V means that the advantages are most evident only for low substitution levels and high current densities. In addition, the increase in first-cycle irreversible capacity seen in Li cells as the Al content in LiNi_{1/3}Co_{1/3-y}Al_yMn_{1/3}O₂ is raised (Fig. 13) also suggests that y should be kept low for the ideal high-rate, high-energy system.

Conclusions

Several materials based on the LiNi_{1/3}Co_{1/3-y}M_yMn_{1/3}O₂ (M = Co, Ti, Al, Fe) system have been synthesized using the GNC method. The electrochemical behavior in lithium cells of electrodes

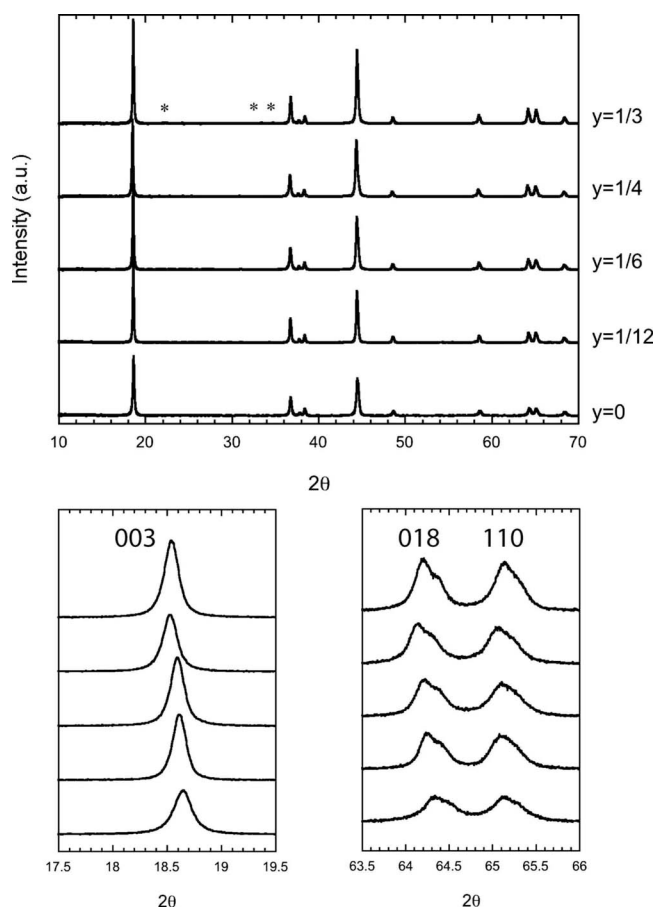


Figure 8. Powder XRD diffraction patterns of $\text{LiNi}_{1/3}\text{Co}_{1/3-x}\text{Al}_x\text{Mn}_{1/3}\text{O}_2$, ($0 \leq y \leq 1/3$) compounds. All materials were single phase except $y = 1/3$, in which an impurity of $\gamma\text{-LiAlO}_2$ (*) is observed. Insets show the consistent shift in the 003 peak and increased 018/110 peak splitting. This implies improved lamellar character with increased Al content.

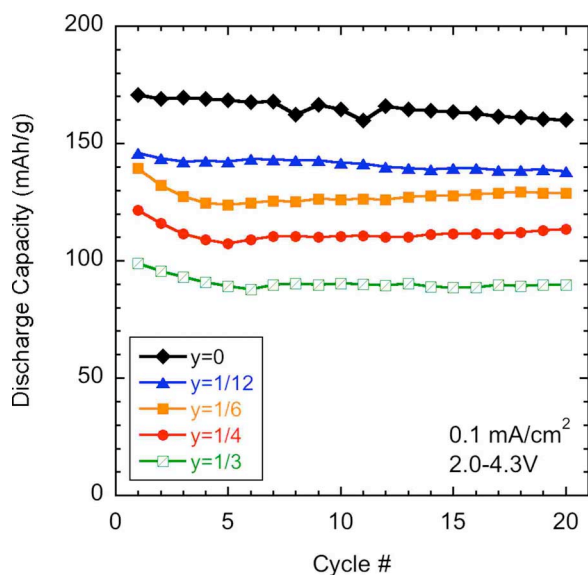


Figure 9. (Color online) Discharge capacities of $\text{Li/LiNi}_{1/3}\text{Co}_{1/3-x}\text{Al}_x\text{Mn}_{1/3}\text{O}_2$, ($0 \leq y \leq 1/3$) cells. Cycling was limited to 2.0–4.3 V vs Li/Li^+ at a constant charge and discharge current density of 0.1 mA/cm^2 .

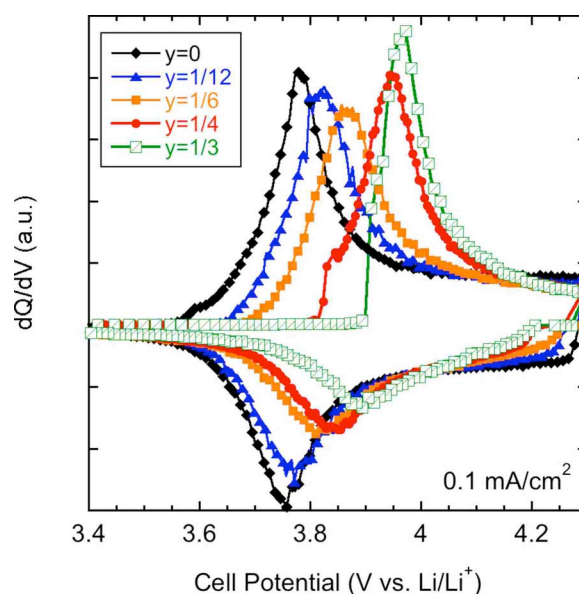


Figure 10. (Color online) Differential capacity plots of the first cycles of $\text{Li/LiNi}_{1/3}\text{Co}_{1/3-x}\text{Al}_x\text{Mn}_{1/3}\text{O}_2$, ($0 \leq y \leq 1/3$) cells. Current density was 0.1 mA/cm^2 in the potential range of 2.0–4.3 V vs Li/Li^+ .

based on these materials is substantially altered compared to the $\text{LiNi}_{1/3}\text{Co}_{1/3}\text{Mn}_{1/3}\text{O}_2$ parent. These differences can be directly attributed to changes in the structural characteristics induced by the substitutions. $\text{LiNi}_{1/3}\text{Co}_{1/4}\text{Fe}_{1/12}\text{Mn}_{1/3}\text{O}_2$ exhibits lower capacity and poorer rate capabilities due to kinetic limitations resulting from an increase in the antisite cation defect concentration as implied by a reduced $c/3a$ ratio. Phase pure $\text{LiNi}_{1/3}\text{Co}_{1/3-y}\text{Al}_y\text{Mn}_{1/3}\text{O}_2$ compounds are formed for $0 \leq y \leq 1/4$, but a $\gamma\text{-LiAlO}_2$ impurity is observed for $y = 1/3$. Although Al substitution results in decreased capacity between 4.3 and 2.0 V when electrodes are discharged in lithium cells, capacity retention and rate capability are substantially improved. This can be attributed to decreased antisite mixing and an increased Li slab dimension compared to $\text{LiNi}_{1/3}\text{Co}_{1/3}\text{Mn}_{1/3}\text{O}_2$.

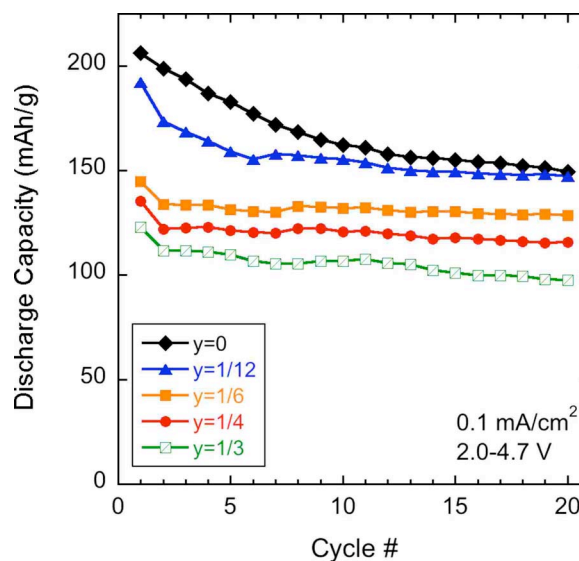


Figure 11. (Color online) Discharge capacities of $\text{Li/LiNi}_{1/3}\text{Co}_{1/3-x}\text{Al}_x\text{Mn}_{1/3}\text{O}_2$, ($0 \leq y \leq 1/3$) cells. Cycling was limited to 2.0–4.7 V vs Li/Li^+ at a constant charge and discharge current of 0.1 mA/cm^2 .

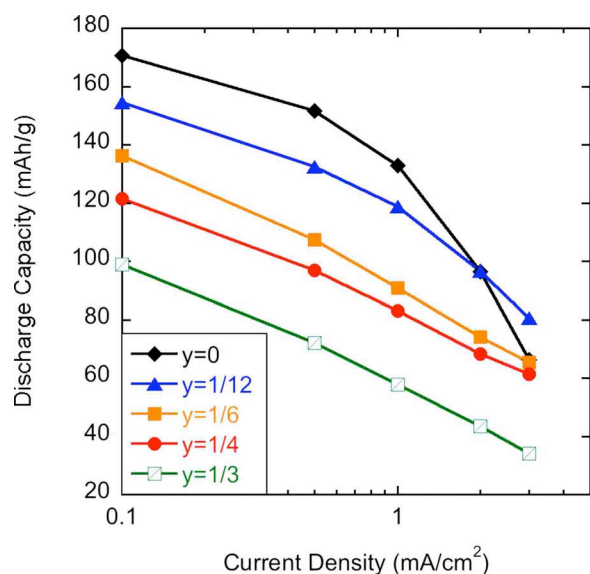


Figure 12. (Color online) Rate capabilities of $\text{Li/LiNi}_{1/3}\text{Co}_{1/3-x}\text{Al}_x\text{Mn}_{1/3}\text{O}_2$, ($0 \leq y \leq 1/3$) cells. Cycling was limited to 2.0–4.3 V and a constant charge current density of 0.1 mA/cm^2 was used.

$\text{LiNi}_{1/3}\text{Co}_{1/4}\text{Ti}_{1/12}\text{Mn}_{1/3}\text{O}_2$ is particularly noteworthy as a high-capacity, high-rate positive electrode material with good stability and very low irreversible capacity loss.

Acknowledgment

This work was supported by the Assistant Secretary for Energy Efficiency and Renewable Energy, Office of Vehicle Technologies of the U.S. Department of Energy under contract no. DE-AC02-05CH11231.

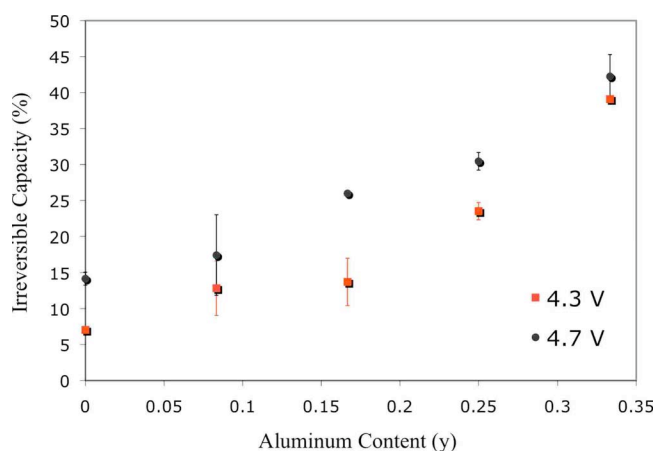


Figure 13. (Color online) Irreversible capacities of $\text{Li/LiNi}_{1/3}\text{Co}_{1/3-x}\text{Al}_x\text{Mn}_{1/3}\text{O}_2$, ($0 \leq y \leq 1/3$) cells cycled to a charge cutoff potential of either 4.3 or 4.7 V (0.1 mA/cm^2 current density).

Lawrence Berkeley National Laboratory assisted in meeting the publication costs of this article.

References

1. T.-H. Cho, Y. Shiosaki, and H. Noguchi, *J. Power Sources*, **159**, 1322 (2006).
2. J. P. B. Amundsen, *Adv. Mater. (Weinheim, Ger.)*, **13**, 943 (2001).
3. N. Yabuuchi, Y. Koyama, N. Nakayama, and T. Ohzuku, *J. Electrochem. Soc.*, **152**, A1434 (2005).
4. T. Ohzuku and Y. Makimura, *Chem. Lett.*, **30**, 642 (2001).
5. N. Yabuuchi and T. Ohzuku, *J. Power Sources*, **119–121**, 171 (2003).
6. Y. Koyama, N. Yabuuchi, I. Tanaka, H. Adachi, and T. Ohzuku, *J. Electrochem. Soc.*, **151**, A1545 (2004).
7. N. Yabuuchi, Y. Makimura, and T. Ohzuku, *J. Electrochem. Soc.*, **154**, A314 (2007).
8. I. Belharouak, Y. K. Sun, J. Liu, and K. Amine, *J. Power Sources*, **123**, 247 (2003).
9. I. Belharouak, W. Q. Lu, D. Vissers, and K. Amine, *Electrochem. Commun.*, **8**, 329 (2006).
10. Z. H. Lu, L. Y. Beaulieu, R. A. Donaberger, C. L. Thomas, and J. R. Dahn, *J. Electrochem. Soc.*, **149**, A778 (2002).
11. T. Ohzuku and Y. Makimura, *Chem. Lett.*, **30**, 744 (2001).
12. Y. Makimura and T. Ohzuku, *J. Power Sources*, **119**, 156 (2003).
13. R. D. Shannon, *Acta Crystallogr., Sect. A: Cryst. Phys., Diff., Theor. Gen. Crystallogr.*, **32**, 751 (1976).
14. E. J. Wu, P. D. Tepesch, and G. Ceder, *Philos. Mag. B*, **77**, 1039 (1998).
15. K. Kang and G. Ceder, *Phys. Rev. B*, **74**, 094105 (2006).
16. J. K. Ngala, N. A. Chernova, M. Ma, M. Mamak, P. Y. Zavalij, and M. S. Whittingham, *J. Mater. Chem.*, **14**, 214 (2004).
17. M. Yoshio, H. Noguchi, J. Itoh, M. Okada, and T. Mouri, *J. Power Sources*, **90**, 176 (2000).
18. A. Manthiram, J. Choi, and W. Choi, *Solid State Ionics*, **177**, 2629 (2006).
19. K. S. Kang, Y. S. Meng, J. Breger, C. P. Grey, and G. Ceder, *Science*, **311**, 977 (2006).
20. T. A. Hewston and B. L. Chamberland, *J. Phys. Chem. Solids*, **48**, 97 (1987).
21. J. N. Reimers, E. Rossen, C. D. Jones, and J. R. Dahn, *Solid State Ionics*, **61**, 335 (1993).
22. Y. S. Meng, Y. W. Wu, B. J. Hwang, Y. Li, and G. Ceder, *J. Electrochem. Soc.*, **151**, A1134 (2004).
23. S.-K. Hu, T.-C. Chou, B.-J. Hwang, and G. Ceder, *J. Power Sources*, **160**, 1287 (2006).
24. M. Ganesan, S. Sundararajan, M. V. T. Dhananjeyan, K. B. Sarangapani, and N. G. Renganathan, *Mater. Sci. Eng., B*, **131**, 203 (2006).
25. H.-W. Ha, K. H. Jeong, and K. Kim, *J. Power Sources*, **161**, 606 (2006).
26. M. Tsuda, H. Arai, M. Takahashi, H. Ohtsuka, Y. Sakurai, K. Sumitomo, and H. Kageshima, *J. Power Sources*, **144**, 183 (2005).
27. H. Liu, J. Li, Z. Zhang, Z. Gong, and Y. Yang, *Electrochim. Acta*, **49**, 1151 (2004).
28. H. Arai, M. Tsuda, and Y. Sakurai, *J. Power Sources*, **90**, 76 (2000).
29. L. A. Chick, L. R. Pederson, G. D. Maupin, J. L. Bates, L. E. Thomas, and G. J. Exarhos, *Mater. Lett.*, **10**, 6 (1990).
30. J. Wilcox and M. Doeff, *ECS Trans.*, **11**(29), 27 (2008).
31. C. H. Jung, J. Y. Park, S. J. Oh, H. K. Park, Y. S. Kim, D. K. Kim, and J. H. Kim, *J. Nucl. Mater.*, **253**, 203 (1998).
32. J. Rodriguez-Carvajal, *Physica B*, **192**, 55 (1993).
33. J. Choi and A. Manthiram, *J. Electrochem. Soc.*, **152**, A1714 (2005).
34. Y. W. Tsai, B. J. Hwang, G. Ceder, H. S. Sheu, D. G. Liu, and J. F. Lee, *Chem. Mater.*, **17**, 3191 (2005).
35. S. Patoux, M. Dolle, and M. M. Doeff, *Chem. Mater.*, **17**, 1044 (2005).
36. S. Albrecht, J. Kumpers, M. Kruft, S. Malcus, C. Vogler, M. Wahl, and M. Wohlfahrt-Mehrens, *J. Power Sources*, **119**, 178 (2003).
37. J. K. Ngala, M. M. Natasha, A. Chernova, M. Mamak, P. Y. Zavalij, and M. S. Whittingham, *J. Mater. Chem.*, **14**, 214 (2004).
38. T. Ohzuku, K. Nakura, and T. Aoki, *Electrochim. Acta*, **45**, 151 (1999).
39. M. Guilmard, A. Rougier, M. Grune, L. Croguennec, and C. Delmas, *J. Power Sources*, **115**, 305 (2003).
40. G. Ceder, Y. M. Chiang, D. R. Sadoway, M. K. Aydinol, Y. I. Jang, and B. Huang, *Nature (London)*, **392**, 694 (1998).
41. J. P. Peres, C. Delmas, A. Rougier, M. Broussely, F. Pertion, P. Biensan, and P. Willmann, *J. Phys. Chem. Solids*, **57**, 1057 (1996).
42. C. Delmas, J. P. Peres, A. Rougier, A. Demourgues, F. Weill, A. Chadwick, M. Broussely, F. Pertion, P. Biensan, and P. Willmann, *J. Power Sources*, **68**, 120 (1997).
43. J. Choi and A. Manthiram, *Electrochem. Solid-State Lett.*, **8**, C102 (2005).
44. J. R. Mueller-Neuhaus, R. A. Dunlap, and J. R. Dahn, *J. Electrochem. Soc.*, **147**, 3598 (2000).
45. S. Patoux and M. M. Doeff, *Electrochem. Commun.*, **6**, 767 (2004).
46. S. Buta, D. Morgan, A. Van der Ven, M. K. Aydinol, and G. Ceder, *J. Electrochem. Soc.*, **146**, 4335 (1999).
47. M. Guilmard, C. Pouillier, L. Croguennec, and C. Delmas, *Solid State Ionics*, **160**, 39 (2003).
48. F. Zhou, X. Zhao, Z. Lu, J. Jiang, and J. R. Dahn, *Electrochem. Commun.*, **10**, 1168 (2008).
49. F. Zhou, X. Zhao, Z. Lu, J. Jiang, and J. R. Dahn, *Electrochem. Solid-State Lett.*, **11**, A155 (2008).